

1 REVISION 1

2 **Mechanism and kinetics of the pseudomorphic replacement of anhydrite by calcium**  
3 **phosphate phases at hydrothermal conditions**

4

5 **Ana Roza-Llera<sup>1</sup>, Amalia Jiménez<sup>1</sup> and Lurdes Fernández-Díaz<sup>2</sup>.**

6 <sup>1</sup> Department of Geology, University of Oviedo, 33005 Oviedo Spain; rozaana@uniovi.es,  
7 amjimenez@uniovi.es

8 <sup>2</sup> Dpto. Cristalografía y Mineralogía, Universidad Complutense de Madrid, José Antonio  
9 Novais, 2, E-28040 Madrid, Spain; ishtar@ucm.es

10 \* Correspondence: amjimenez@uniovi.es

11

12 **Abstract**

13 Mineral replacement reactions mediated by fluids are common in sedimentary basins, where  
14 they influence geochemical cycles. Phosphorous (P) pollution of soils, sediments and water  
15 bodies is currently a widespread problem. Some apatite accumulations in sediments may have  
16 formed through the interaction of P-bearing aqueous solutions with mineral surfaces that result  
17 in mineral replacement reactions. Here, we investigate the pseudomorphic replacement of  
18 anhydrite single crystals by aggregates of  $\beta$ -tricalcium phosphate and hydroxyapatite upon  
19 interaction with a P-bearing solution at temperatures between 120°C and 200°C. SEM  
20 imaging is used to study the texture of the aggregates. Rietveld refinement of the X-ray  
21 diffraction patterns and Raman spectra analysis of the reacted samples provide information on  
22 the kinetics of the replacement. At all temperatures  $\beta$ -tricalcium phosphate forms alongside  
23 hydroxyapatite at early stages of the replacement reaction. At  $T \geq 180^\circ\text{C}$ , hydroxyapatite/ $\beta$ -

24 tricalcium phosphate ratio rapidly increases, and hydroxyapatite is the only phase in fully  
25 replaced samples. At  $T < 180^{\circ}\text{C}$  hydroxyapatite/ $\beta$ -tricalcium phosphate ratio increases slowly  
26 and fully replaced samples still contain significant amounts of  $\beta$ -tricalcium phosphate. The  
27 progress of the replacement is facilitated by the formation of porosity. The evolution of the  
28 hydroxyapatite/ $\beta$ -tricalcium phosphate ratio and the crystal habit of both phases strongly  
29 influence the arrangement of this porosity. The empirical activation energy  $E_a$  (kJ/mol) of the  
30 replacement reaction is determined by the Avrami and the iso-conversion methods. Both  
31 approaches yield an  $E_a$  of  $\sim 40$  kJ/mol. Anhydrite dissolution appears as the rate-limiting  
32 process and the overall kinetics of the replacement reaction is controlled by the rate diffusion  
33 of dissolved species through the porosity network. The ripening of the metastable  $\beta$ -tricalcium  
34 phosphate into hydroxyapatite affects the characteristics of the porosity network and further  
35 modulates the kinetics of the replacement. These results may improve the understanding of  
36 the mechanisms of P-sequestration by mineral surfaces through coupled dissolution–  
37 precipitation reactions and shed light on the origin of apatite accumulations associated to  
38 evaporitic sedimentary rocks.

39 **Keywords:** anhydrite, hydroxyapatite,  $\beta$ -tricalcium phosphate, mineral replacement,  
40 pseudomorphism, kinetics, textures, coupled dissolution–precipitation.

41

## 42 **Introduction**

43 Mineral replacements are common processes in sedimentary, diagenetic, metamorphic, and  
44 metasomatic environments, where they take place mediated by a fluid that facilitates the  
45 dissolution of the primary mineral and the concomitant precipitation of the secondary one(s).  
46 The coupling through the interface of the dissolution and precipitation rates allows for the  
47 preservation of original shape and volume of the primary mineral (Putnis 2002, 2009; Putnis

48 and Putnis 2007; Pollok et al. 2011; Ruiz-Agudo et al. 2014). Moreover, when the dissolution  
49 of the latter is the rate-limiting step of the interface coupled dissolution-precipitation reaction  
50 (ICDP), original microscopic, and even nanoscopic, features also are accurately preserved  
51 during the replacement (Xia et al. 2009; Ruiz-Agudo et al. 2014; Altree-Williams et al. 2015).  
52 The progress of ICDP reactions requires a continuous communication between the interface,  
53 where the reaction takes place, and the bulk fluid. This communication is ensured by the  
54 formation of a network of porosity and/or fractures during the mineral replacement. This  
55 network facilitates mass transport to and from the interfacial fluid (Zhao et al. 2009; Jonas et  
56 al. 2013; Ruiz-Agudo et al. 2014; Putnis 2015).

57 In this work we describe the replacement of anhydrite by mixtures of two calcium phosphate  
58 phases,  $\beta$ -tricalcium phosphate ( $\beta$ -Ca<sub>3</sub>(PO<sub>4</sub>)<sub>2</sub>) ( $\beta$ -TCP) and hydroxyapatite (Ca<sub>5</sub>(PO<sub>4</sub>)<sub>3</sub>(OH))  
59 (Hap) through a ICDP mediated by an aqueous fluid containing phosphorous (P). Anhydrite  
60 is a rock-forming mineral common in sedimentary basins, where it appears as a major  
61 component of evaporites as well as forming nodules and cements in sandstones, limestones  
62 and dolostones (Murray 1964; Rahimpour-Bonab et al. 2010; Olivarius et al. 2015).  
63 Anhydrite also forms massive accumulations in modern submarine hydrothermal vents (Kuhn  
64 et al. 2003). Apatite (Ca<sub>5</sub>(PO<sub>4</sub>)<sub>3</sub>(OH,Cl,F)) is the main source of phosphorous, an element  
65 that is scarce in the Earth's crust but has great economic interest in the fertilizer industry  
66 (Filippelli 2002). Phosphorous is an essential macronutrient for biota as well as a pollutant  
67 which in excess causes eutrophication of water bodies, contributes to the growth of toxigenic  
68 algae, and boosts the development of potentially pathogenic microbes in the water column  
69 and in soils (Mallin and Cahoon 2020). The structural characteristics of apatite make it a  
70 relevant phase for immobilizing and storing of radioactive and other pollutant elements  
71 (Rakovan and Reeder 1996; Ewing and Wang 2002; Mavropoulos et al. 2002).

72 There is abundant evidence that mineral replacement reactions play an important role in  
73 controlling the fate of a variety of pollutants in soils and sedimentary basins (Pinto et al. 2009,  
74 2012; Wang et al. 2012, 2015; Hövelmann and Putnis 2016; Callagon et al. 2017; Di Lorenzo  
75 et al. 2019; Roza Llera et al. 2021). Anhydrite is highly reactive to dissolved ions. Thus, cycles  
76 of anhydrite dissolution/precipitation influence the fate of trace elements (Sr, Y, REE) in  
77 hydrothermal systems. Moreover, anhydrite surfaces effectively remove metal pollutants from  
78 aqueous solutions through coprecipitation phenomena (Morales et al. 2014; Forjanés et al.  
79 2020b, 2020a). Pollution of running waters and aquifers by phosphorous currently is  
80 widespread due to the extensive use of ammonium phosphate as a fertilizer in intensive  
81 agriculture (Smith 2003; Wei and Bailey 2021). Understanding the processes that result from  
82 the interaction of phosphorous containing waters with common sedimentary rock-forming  
83 minerals can help to mitigate the effects of phosphorous pollution in sedimentary basins.

84 Moreover, apatite is a main constituent of sedimentary phosphorites (Bentor 1980; Sheldon  
85 1981; Hughes et al. 1989; Knudsen and Gunter 2002). Baturin (1989) reported on the  
86 diagenetic origin of some apatite accumulations and connected their formation to changes in  
87 the chemistry of pore waters due to organic matter decay and sulfate reduction. The  
88 concentration of phosphorous in diagenetic fluids in pores can reach values up to 8-9 mg/L,  
89 according to Sheldon (1981). Filippelli (2002) and Dzombak and Sheldon (2020) have  
90 reported that P concentrations in young soils can reach values as high as 5340 mg/L,  
91 highlighting the potential importance of P fluxes from soils to rivers in the current scenario of  
92 climate change. In contact with the surface of sediment particles, these high concentrations  
93 are sufficient to guarantee the precipitation of apatite, which opens the question of the role  
94 that interface coupled dissolution-precipitation reactions (ICDP) may play in the formation of  
95 diagenetic apatite. It has been experimentally demonstrated that the interaction of phosphate-  
96 bearing fluids with other sedimentary rock-forming minerals like aragonite and calcite results

97 in their replacement by aggregates of apatite crystals (Kasioptas et al. 2010, 2011; Jonas et al.  
98 2013; Reinares-Fisac et al. 2017).

99 The purpose of the present work is to study the interaction of a P-bearing aqueous solution  
100 with anhydrite single crystals. The main goal is to determine the kinetics and mechanisms of  
101 anhydrite replacement by calcium phosphate at temperatures between 120°C and 200°C. Two  
102 calcium phosphate phases,  $\beta$ -TCP ( $\beta$ -Ca<sub>3</sub>(PO<sub>4</sub>)<sub>2</sub>) and Hap (Ca<sub>5</sub>(PO<sub>4</sub>)<sub>3</sub>(OH)), formed during  
103 this replacement, which were identified by Raman spectroscopy and X-ray powder diffraction  
104 (XRD). The amount of each phase as a function of temperature and reaction time was  
105 calculated by conducting the Rietveld analysis of the X-ray diffraction (XRD) patterns. This  
106 information was applied to determine the kinetics of the process. The textural relationships  
107 and the crystal habit of the product phases were studied by scanning electron microscopy  
108 (SEM). The influence of the transformation of  $\beta$ -TCP into Hap, which occurs concomitantly  
109 to the progress of the replacement, as well as the specific morphological and textural features  
110 of both calcium phosphates in the overall kinetics of the replacement reaction, was considered.

111

## 112 **Materials and methods**

### 113 **Hydrothermal experiments**

114 Hydrothermal interaction experiments were performed by reacting anhydrite single crystals  
115 with a 2M (NH<sub>4</sub>)<sub>2</sub>HPO<sub>4</sub> aqueous solution at different reaction times (1 h to 5 days) and  
116 temperatures (120, 150, 180 and 200°C) under autogenous pressure. The P concentration in  
117 the aqueous solution is around 10 times higher than that reported in young soils (Filippelli  
118 2002; Dzombak and Sheldon 2020). Anhydrite single crystals from Naica mine (Chihuahua,  
119 México) were used in all experiments. X-ray fluorescence spectroscopic analysis confirmed  
120 them as highly, with less than 0.4 wt% foreign elements and Sr as the major impurity. The

121 anhydrite crystals were cleaved along {100}, {010} and {001} using a sharp stainless-steel  
122 knife edge to obtain similarly sized (about 3 x 3 x 3 mm) anhydrite subsamples. Prior to their  
123 use in the experiments, these subsamples were cleaned in an ethanol bath to remove surface  
124 impurities and then left to dry overnight in a desiccator at room temperature. Four anhydrite  
125 subsamples (average weight  $\sim 250 \pm 1$  mg) were used in each experiment, and the volume of  
126 the solution ( $\sim 4$  mL) was adjusted to guarantee a solid-to-liquid ratio of 0.06 g/mL. Anhydrite  
127 subsamples were placed together with the P-bearing aqueous solution in pre-heated individual  
128 stainless-steel Teflon-lined autoclaves (2.5  $\varnothing$  x 10 cm). Within the autoclave, all four  
129 anhydrite subsamples laid with one of their surfaces in contact with the bottom of the reactor,  
130 while their other five surfaces were directly exposed to the interaction with the P-bearing  
131 solution. The crystallographic orientation of the laying surface was not taken into  
132 consideration when setting the different experimental runs. The P-bearing aqueous solution  
133 was prepared by dissolving reagent-grade  $(\text{NH}_4)_2\text{HPO}_4$  (Acros Organics) in high purity  
134 deionized water (MilliQ) (18 M $\Omega$  cm). The pH of the fluid was measured prior to and after  
135 reaction by using a pH Meter basic 20-CRISON. Experiments were run triplicated to confirm  
136 reproducibility. The aqueous solutions were modeled using the geochemical code PHREEQC  
137 (Parkhurst and Appelo 1999) and llnl.dat database to calculate saturation indexes (SI) with  
138 respect to relevant solid phases at the beginning of the experiments.

139 After reaction, the autoclaves were removed from the oven. To accelerate their cooling to  
140 room temperature (25°C) a flow of compressed air was applied during 20 minutes. The  
141 reaction time does not comprise this cooling period. Afterwards, the product samples were  
142 removed from the solution, washed with distilled water, and dried overnight at 30°C in a  
143 thermostatic chamber. Two of the four product samples from each experiment were powdered  
144 in an agate mortar and used for powder X-ray diffraction (XRD) analyses. The other two

145 product samples were crosscut using a steel cutter and used for Raman spectroscopy and  
146 scanning electron microscopy (SEM) imaging analyses.

### 147 **Analytical methods**

148 Diffraction patterns of powdered product samples were measured at room temperature with a  
149 PANalytical Xpert Pro diffractometer, using a  $\text{CuK}\alpha 1$  radiation. XRD data were collected in  
150 the range  $7\text{--}90^\circ 2\theta$  with a step size of  $0.001^\circ$  and a dwell time of 1 s per step. Samples were  
151 hold in thin-walled glass capillaries to minimize preferential orientation effects. General peak  
152 matching runs were conducted for the diffraction patterns of product samples. These runs  
153 confirmed that in all diffraction patterns all peaks could be assigned to anhydrite (PDF 98-  
154 900-1234) and/or Hap (PDF 98-006-8592) and  $\beta$ -TCP (PDF 00-009-0169). Furthermore,  
155 anhydrite, Hap and  $\beta$ -TCP fractions in the reacted samples were determined by performing  
156 Rietveld refinement analyses using the X'Pert HighScore Plus (Version 3.0) software package  
157 from PANalytical. The aforementioned structural models were used as references.

158 Crosscut reacted samples were gold-coated and imaged using a JEOL-6610LV microscope  
159 equipped with Energy-dispersive X-ray spectroscopy (EDX, INCA Energy 350). The contrast  
160 resulting from the different composition of reacted and unreacted areas provided information  
161 on the progresses of the anhydrite-(P)-bearing fluid interaction. Secondary electron images of  
162 the external surfaces of the reacted solid samples were also obtained.

163 Raman spectra were collected from freshly crosscut sections of the reacted subsamples.  
164 Raman spectroscopy was performed by means of a labRam HRU using JYVJobin Yvon  
165 equipment with an excitation source laser CDPS532-DPSS at 24.3 mW and excitation times  
166 of 10 s. This equipment was connected to a confocal microscope Olympus BXFM-ILHS with  
167 a 100x objective.

### 168 **Kinetic analysis**

169 We assume that the isothermal kinetics of the anhydrite phosphation reaction can be described  
170 by the Avrami equation (Eq.1):

$$171 \quad y_{CaP} = 1 - e^{-(kt)^n} \quad (1)$$

172 where  $y_{CaP}$  corresponds to the fraction of calcium phosphate formed ( $y_{Anh} = 1 - y_{CaP}$ ), this is the  
173 extent of the phosphation reaction,  $t$  (hours) represents the reaction time,  $k$  is the Avrami rate  
174 constant ( $\text{hour}^{-1}$ ) and  $n$  is the Avrami exponent. By linearizing the Avrami equation taking  
175 twice natural logarithms the following expression is obtained:

$$176 \quad \ln(-\ln(1 - y_{CaP})) = n \ln k + n \ln t \quad (2)$$

177 The Avrami equation has successfully been used to describe the kinetics of a variety of  
178 dissolution, crystallization, transformation, and mineral replacement processes (Lasaga 1998;  
179 Xia et al. 2009; Kasiotas et al. 2010; Altree-Williams et al. 2017; Pedrosa et al. 2017). If a  
180 reaction follows the Avrami equation, different isokinetic curves will have the same  $n$  value.  
181 Moreover, their plot as  $\ln(-\ln(1 - y_{CaP}))$  against  $\ln t$  (Hancock-Sharp plot) will show  
182 approximately equal gradients (Hancock and Sharp 1972). Changes in the value of  $n$  are  
183 indicative of changes in the mechanisms of the reaction. If the activation energy of the reaction  
184 is constant, the Hancock-Sharp plot will yield a straight line, whose slope corresponds to the  
185 value of  $n$  and from whose intercept with the  $y$ -axis the rate constant  $k$  can be estimated.  
186 Deviations from linearity of the Hancock-Sharp plot indicate that the reaction equation differs  
187 from the Avrami one.

188 The rate constant  $k$  of most reactions shows a dependence of temperature that follows an  
189 Arrhenius type equation:

$$190 \quad k = A \cdot e^{\frac{-Ea}{R \cdot T}} \quad (3)$$

191 where  $A$  is a frequency factor,  $R$  is the gas constant,  $T$  is the temperature of the experiment  
192 (Kelvin) and  $E_a$  is the empirical activation energy. Taking logarithm, the equation 4 is  
193 obtained:

$$194 \quad \ln k = \ln A - E_a/RT \quad (4)$$

195 If  $A$  and  $E_a$  are constant, the plot of  $\ln k$  versus  $1/T$  is a straight line whose slope is  $E_a/R$  and  
196 its intercept with the y-axis is  $\ln A$ . Thus, the value of  $E_a$  can be estimated using the rate  
197 constants  $k$  derived from the Hancock-Sharp plots of a set of isothermal runs.

198 Commonly the empirical activation energy sums up contributions of different events involved  
199 in the reaction (dissolution of primary phases, mass transfer through interfaces, ion  
200 dehydration, nucleation and growth of secondary phases, etc). Moreover, the method  
201 described above fails to reveal changes in the activation energy that occur as the reaction  
202 progresses. It is possible to derive information on the evolution of the empirical activation  
203 energy  $E_a$  along the reaction by rewriting equation 1 and calculating the time required to  
204 achieve the transformation of a given fraction of the primary phase, in this case, anhydrite,  
205 into the secondary phase(s), in this case, Hap and  $\beta$ -TCP or a mixture of both phases,  
206 according to equation 5:

$$207 \quad t_Y \propto k^{-1} \propto A^{-1} e^{\frac{E_a}{RT}} \quad (5)$$

208 where  $t_Y$  is the time for a given fraction to transform. This approach is described as the  
209 isoconversional method or the time to a given fraction method (Putnis 1992).

210 Taking logarithms, equation 5 can be rearranged as:

$$211 \quad \ln t_Y = \text{const} - \ln A + E_a/RT \quad (6)$$

212 Empirical activation energies can be derived by plotting  $\ln t_Y$  versus  $1/T$ . If there is no change  
213 in the reaction mechanism as the reaction progresses, all plots will have similar gradients and,

214 consequently,  $E_a$  will have a constant value, regardless of the given fraction transformed. On  
215 the contrary, changes in plot slopes are indicative of different mechanisms operating at  
216 different stages of the reaction, each one characterised by a different  $E_a$ .

217

## 218 **Results**

### 219 **Reaction Pathway and Textural Features**

220 The hydrothermal interaction of anhydrite single crystals with a phosphate-bearing aqueous  
221 solution (2M  $(\text{NH}_4)_2\text{HPO}_4$ ) results in their partial to total transformation into Hap  
222 ( $\text{Ca}_5(\text{PO}_4)_3(\text{OH})$ ). Hydroxyapatite can be accompanied by varying amounts of  $\beta$ -TCP ( $\beta$ -  
223  $\text{Ca}_3(\text{PO}_4)_2$ ) depending on the temperature and duration of the interaction. During the  
224 transformation, the pH of the solutions progressively decreases from an initial value of 8.1 (1)  
225 to 6.8 (1) at experiment termination time. Figure 1a depicts the XRD patterns from subsamples  
226 reacted during 6 to 72 h at 120°C. All the diffraction patterns show sharp peaks that can be  
227 assigned to anhydrite and/or the calcium phosphate phases Hap and  $\beta$ -TCP. Although the  
228 XRD patterns of other calcium phosphates like whitlockite ( $\text{Ca}_{18}(\text{Mg,Fe})_2\text{H}_2\text{PO}_4$ )<sub>14</sub>) show  
229 similar features as the pattern of  $\beta$ -TCP (Gopal and Calvo 1972; Jonas et al. 2014), the  
230 formation of any amount of the former phase is disregarded, since the pristine anhydrite is  
231 highly pure and the aqueous phase contains no dissolved Fe and Mg. The intensity of anhydrite  
232 peaks progressively decreases with the reaction time. Anhydrite peaks are absent in the pattern  
233 corresponding to a reaction time of 72 h. Conversely, the intensity of peaks assigned to Hap  
234 progressively increases with time. Peaks assigned to  $\beta$ -TCP show a more complex evolution:  
235 their intensity initially grows to latter decrease. In all the experiments, regardless of the  
236 reaction temperature, Hap rapidly becomes the main constituent of the transformed fraction.  
237 For example, in experiments conducted at 120°C, the transformed fraction contains ~ 20 wt%

238 Hap after 12 h, 37 wt% Hap after 24 h and 73 wt% Hap after 48 h (Fig. 1b). In experiments  
239 conducted at temperatures  $\geq 200^{\circ}\text{C}$ , Hap becomes the only solid phase present in the system  
240 after 10 h since the beginning of the experiment. In addition, longer experiments were carried  
241 out at temperatures below  $180^{\circ}\text{C}$ , once the anhydrite had been completely replaced, to observe  
242 the evolution of the relative content of  $\beta$ -TCP and Hap in the samples. The results of these  
243 experiments indicated that the amount of  $\beta$ -TCP continued to decrease with time. After 5 days  
244 interaction at  $120^{\circ}\text{C}$ , reacted samples consist of 7.2%  $\beta$ -TCP and 92.8 anhydrite. The Raman  
245 spectra collected on crosscut sections of reacted anhydrite subsamples indicate that all  
246 transformed rims exclusively consist of calcium phosphate phases in good agreement with the  
247 conclusions of XRD analyses. Figure 2 shows SEM images and Raman spectra taken on  
248 crosscut sections of anhydrite reacted with the P-bearing fluid at  $150^{\circ}\text{C}$  during 12 h (Figs. 2a-  
249 2d) and 24 h (Figs. 2e-2h). The spectrum in Figure 2a shows the main vibration bands of  $\text{SO}_4^{2-}$   
250 in anhydrite: a symmetric stretching ( $\nu_1$ ) band at  $1019\text{ cm}^{-1}$ , three asymmetric stretching ( $\nu_3$ )  
251 bands at  $1113\text{ cm}^{-1}$ ,  $1131\text{ cm}^{-1}$  and  $1160\text{ cm}^{-1}$ , two symmetric bending ( $\nu_2$ ) bands at  $416\text{ cm}^{-1}$   
252 and  $502\text{ cm}^{-1}$ , and three asymmetric bending ( $\nu_4$ ) bands at  $610\text{ cm}^{-1}$ ,  $627\text{ cm}^{-1}$  and  $678\text{ cm}^{-1}$ .  
253 Raman spectra collected from transformed regions of samples reacted during 12 h (Fig. 2c)  
254 and 24 h (Figs. 2e and 2g) show bands that can be assigned to Hap: the symmetric stretching  
255 ( $\nu_1$ ), the symmetric bending ( $\nu_2$ ) and the asymmetric bending ( $\nu_4$ ) vibration modes of  $\text{PO}_4^{3-}$   
256 are located at  $961\text{ cm}^{-1}$ ,  $432\text{ cm}^{-1}$  and  $588\text{ cm}^{-1}$ , respectively. The presence of a minor broad  
257 band around  $880\text{ cm}^{-1}$  (Figs. 2c and 2e) that can be attributed to the P-OH stretching is also  
258 consistent with Hap (Penel et al. 1998). Moreover, a triplet at  $1007$ ,  $1045$  and  $1075\text{ cm}^{-1}$ ,  
259 corresponds to the  $\text{PO}_4^{3-}$  asymmetric stretching ( $\nu_3$ ) as well as a band at  $3571\text{ cm}^{-1}$  can be  
260 assigned to the OH-stretching (Fig. 2). In addition, a broad band near  $946\text{--}949\text{ cm}^{-1}$  assigned  
261 to the symmetric stretching ( $\nu_1$ ) (Jonas et al. 2014; Pedrosa et al. 2016) indicates the presence  
262 of  $\beta$ -TCP in the core of the sample reacted during for 24 h (Fig. 2e). The absence of bands

263 around  $925\text{ cm}^{-1}$  ( $\nu_1$  mode) in all Raman spectra, confirms that whitlockite is not present in  
264 the system at any stage, in good agreement with the results of XRD analyses that only identify  
265 two calcium phosphate phases ( $\beta$ -TCP and Hap).

266 The main  $\text{PO}_4^{3-}$  vibrational mode ( $\nu_1$ ) in  $\beta$ -TCP, which is located at  $971\text{ cm}^{-1}$ , is not apparent  
267 in any of the Raman spectra, most likely due to overlapping with the main band in the spectra  
268 of Hap ( $\text{PO}_4^{3-}$   $\nu_1$  at  $961\text{ cm}^{-1}$ ). No bands that can be attributed to  $\beta$ -TCP are present in areas  
269 close to the surface of the anhydrite sample reacted during 24 h (Fig. 2g). In summary, XRD  
270 and Raman results corroborate that the transformed samples consist of mixtures of Hap and  
271  $\beta$ -TCP at early stages of the replacement reaction. At  $T \geq 180^\circ\text{C}$ , hydroxyapatite/ $\beta$ -tricalcium  
272 phosphate ratio rapidly increases, and hydroxyapatite is the only phase in fully replaced  
273 samples. At  $T < 180^\circ\text{C}$  hydroxyapatite/ $\beta$ -tricalcium phosphate ratio increases slowly.  
274 Furthermore, reacted samples still contain significant amounts of  $\beta$ -tricalcium phosphate even  
275 after full replacement of anhydrite is reached.

276 The anhydrite by calcium phosphate replacement initiates at the surface of the anhydrite  
277 subsamples and advances inwards, defining a sharp reaction front (Figs. 2b and 2d). This front  
278 defines the interface between a shell-like transformed rim and the unreacted anhydrite core  
279 (Fig. 2d). Figure 3a shows the contact between the transformed rim and the unreacted  
280 anhydrite core. As can be seen, the rim mainly consists of needle-like crystals arranged in  
281 fan-like bunches that appear oriented roughly perpendicular to the surface of the anhydrite  
282 core, and a smaller amount of euhedral rhombohedron-shaped crystals (Fig. 3a). Based on  
283 Raman spectroscopy analysis and the known crystal morphology of calcium phosphates, we  
284 interpret the needle-like crystals as Hap (Zhu et al. 2008; Kasiopas et al. 2010; Yang et al.  
285 2014; Li et al. 2016) and the euhedral rhombohedron-shaped ones as  $\beta$ -TCP (Roy and  
286 Linnehan 1974). Closer inspection of the latter evidences the presence on their surfaces of

287 dissolution pits and nanometric Hap crystals that appear to grow in close spatial relation with  
288 the dissolution pits (Fig. 3b).

289 Regardless the reaction temperature, the replacement reaction takes place with preservation  
290 of both the volume and external shape of the anhydrite crystals and results in the formation of  
291 calcium phosphate pseudomorphs. The pseudomorphs obtained in series of isothermal  
292 experiments were crosscut and SEM imaged. Figure 4 depicts SEM microphotographs of  
293 samples reacted during 12 hours at 120°C (a), 150°C (b), 180°C (c) and 200°C (d). The  
294 transformed rim undergoes progressive thickening with increasing reaction time. The  
295 anhydrite core concomitantly shrinks. It is important to note that, before full anhydrite  
296 replacement is reached, the thickness of the transformed rim can significantly vary within each  
297 crosscut section, as is apparent in Figures 4a-4c. Differences in rim thickness, measured from  
298 opposite sides of a subsample along the same crystallographic direction, reflect the reduced  
299 exposure of the subsample surface that lies in contact with the reactor bottom to the interaction  
300 with the fluid. Differences in rim thickness measured along different crystallographic  
301 directions reflect the different reactivity of anhydrite cleavage surfaces.

302 As can be seen, the reaction front advances faster with increasing temperature. Thus, after 12  
303 h of reaction, in samples reacted at 120°C and 150°C and 180°C, the average transformed rim  
304 thickness was 250, 550 and 1500  $\mu\text{m}$ , respectively (Figs. 4a-4c). After 12 h reaction, no  
305 unreacted core is observed in the crosscut sections of samples from experiments conducted at  
306 200°C reacted (Fig. 4d). This is consistent with the results of both, X-ray diffraction and  
307 Raman spectroscopy analyses, which also support the complete replacement of anhydrite by  
308 calcium phosphate phases in samples reacted 12 hours at 200°C.

### 309 **Kinetics of the replacement reaction**

310 Several sets of hydrothermal interaction experiments were conducted to derive information  
311 on the kinetics of the replacement of anhydrite single crystals by calcium phosphate crystal

312 aggregates. Table 1 summarises the fraction of anhydrite, Hap and  $\beta$ -TCP, as determined from  
313 the Rietveld refinements of X-ray powder diffraction patterns of samples interacted with the  
314 phosphate-bearing aqueous solution at temperatures between 120°C and 200°C during times  
315 that varied between 2 and 72 hours. In Figure 5, the fraction of sample transformed into  
316 calcium phosphate phases ( $y_{CaP}$ ) is plotted against the reaction time ( $t$ ) for each isothermal  
317 experiment. Figure 6 shows the temperature dependence of the anhydrite-by- calcium  
318 phosphate reaction, evidenced in the Hancock-Sharp plots derived by fitting the linearized  
319 Avrami expression (equation 2) to the experimental data. All fitted lines are approximately  
320 parallels. The Avrami parameters calculated for each set of isothermal data are also shown in  
321 Figure 6. The activation energy can be obtained by plotting the slopes of the linear regressions  
322 in Figure 6 against reciprocal temperature in an Arrhenius plot (Fig. 7). The rate constant ( $k$ )  
323 clearly increases with temperature and the linear regression yields an empirical activation  
324 energy,  $E_a$  of  $40.2 \pm 1.9$  kJ/mol.

325 Alternatively, empirical activation energies can also be determined by using the  
326 isoconversional method.  $E_a$  values were calculated for three different fractions of anhydrite  
327 replacement by calcium phosphate, 0.40, 0.60, and 0.80 (Fig. 8). In all cases, the data are well  
328 described by linear correlations and show closely parallel trends. The empirical  $E_a$  values  
329 yielded from these fittings slightly decreases, from  $40.4 \pm 2.3$  to  $39.3 \pm 2.3$  kJ·mol<sup>-1</sup>, as the  
330 replaced fraction increases from 40 to 80%.

331

## 332 **Discussion**

### 333 **Replacement reaction mechanism**

334 Upon interaction with a P-bearing aqueous solution at temperatures between 120°C and  
335 200°C, anhydrite single crystals are replaced by mixtures of  $\beta$ -TCP and Hap. Textural features

336 of the reacted samples are consistent with the replacement taking place through an interface  
337 coupled dissolution-precipitation reaction (Putnis 2002, 2009; Putnis and Putnis 2007; Ruiz-  
338 Agudo et al. 2014). Firstly, the reaction starts at the surface of anhydrite and progresses from  
339 rim to core through the advancement of a reaction front that appears sharp, well defined, and  
340 approximately parallel to the original anhydrite surface. Secondly, the external shape as well  
341 as most surface features of anhydrite crystals are preserved throughout the reaction, which has  
342 a pseudomorphic character. Thirdly, replaced samples consist of aggregates of crystals of the  
343 product phases and contain large amounts of porosity. All these features are characteristic of  
344 mineral replacement processes that occur mediated by the presence of a fluid phase. The  
345 reaction takes place in the interfacial layer of fluid. When the process starts, the fluid is  
346 undersaturated with respect to the primary phase. This drives its dissolution and determines  
347 that the interfacial layer of fluid soon becomes supersaturated with respect to the product(s).  
348 Anhydrite dissolution releases  $\text{Ca}^{2+}$  and  $\text{SO}_4^{2-}$  ions to the interfacial layer of fluid. To evaluate  
349 the physicochemical conditions in the interfacial fluid at early stages of replacement process  
350 we simulate the dissolution of a small amount of anhydrite in a small volume of fluid using  
351 the geochemical code PHREEQC and the *lnll.dat* database (Parkhurst and Appelo 1999). We  
352 consider the successive dissolution of layers of anhydrite whose thickness corresponds to one  
353 unit cell ( $a_0 = 6.993 \text{ \AA}$ ,  $b_0 = 6.995 \text{ \AA}$  and  $c_0 = 6.245 \text{ \AA}$ ; Hawthorne and Ferguson 1975). For a  
354  $3 \times 3 \times 3 \text{ mm}$  sized crystal the dissolved anhydrite volume is  $3.64 \times 10^{-8} \text{ cm}^3$  of  $\text{CaSO}_4$ , which  
355 corresponds to  $7.94 \times 10^{-10}$  moles of anhydrite. We consider two realistic thickness for the  
356 fluid boundary layer, 100 nm and 1000 nm, which corresponds to a volume of interfacial  
357 solution of  $5.40 \times 10^{-6} \text{ cm}^3$  and  $5.4 \times 10^{-5} \text{ cm}^3$ , respectively (Ruiz-Agudo et al. 2015). The  
358 state of supersaturation is defined by the value of the saturation index (SI), which is expressed  
359 as:

360 
$$\text{SI} = \log (\text{IAP}/\text{K}_{\text{sp}}) \quad (7),$$

361 where IAP is the ion activity product and  $K_{sp}$  is the solubility product of the phase considered.  
362  $SI = 0$  indicates that the system is in equilibrium with a given phase, this is saturated, while  
363  $SI < 0$  and  $SI > 0$  indicate that the system is undersaturated and supersaturated, respectively.  
364 At 150°C, the dissolution of one anhydrite monolayer in both 100 nm and 1000 nm boundary  
365 layers results in the interfacial fluid layer becoming supersaturated with respect to Hap and  $\beta$   
366 -TCP. Thus, the 100 nm thick boundary layer becomes supersaturated with respect to both,  
367 Hap and  $\beta$  -TCP ( $SI_{Hap} = 23.86$ ,  $SI_{\beta-TCP} = 3.42$ ) after the dissolution of one anhydrite  
368 monolayer, while still remaining undersaturated with respect to this latter phase ( $SI_{Anh} = -$   
369 7.36). Similarly, the 1000 nm thick boundary layer reaches supersaturation with respect to  
370 Hap and  $\beta$  -TCP ( $SI_{Hap} = 19.11$ ,  $SI_{\beta-TCP} = 0.56$ ) after the dissolution of one anhydrite  
371 monolayer. The simulation of the dissolution of one anhydrite monolayer at other  
372 experimental temperatures also yields  $SI > 0$  for both, Hap and  $\beta$  -TCP. The SI value for all  
373 the phases involved increases as successive anhydrite monolayers dissolve. Once the  
374 interfacial fluid reaches the supersaturation threshold for Hap and  $\beta$  -TCP nucleation, both  
375 calcium phosphate phases will precipitate at the reaction front. As a replaced rim forms, the  
376 presence of pores within it guarantees a continuous communication between the bulk solution  
377 and the reaction front, facilitating mass transport to and from the interface (Putnis et al. 2005;  
378 Putnis and Putnis 2007; Pollok et al. 2011; Forjanés et al. 2020b). The progress of the reaction  
379 involves the definition of a dissolution-crystallization feedback loop. Thus, anhydrite  
380 dissolution promotes calcium phosphate precipitation in the interfacial fluid and *vice versa*.  
381 The preservation of the external shape of anhydrite crystals requires that the rates of anhydrite  
382 dissolution and calcium phosphate precipitation are coupled (Putnis 2002, 2009; Putnis and  
383 Putnis 2007; Pollok et al. 2011; Ruiz-Agudo et al. 2014). In the temperature range of the  
384 experiments, the solubility product of anhydrite varies between  $10^{-4.36}$  at 120°C and  $10^{-4.83}$  at  
385 200°C (Freyer and Voigt 2003). The solubility product of Hap strongly decreases with

386 increasing temperature within this temperature range, being  $10^{-58.33}$  at 120°C and  $10^{-70.64}$  at  
387 200°C (Kaufman and Kleinberg 1979). In contrast, the solubility product of  $\beta$ -TCP slightly  
388 increases with temperature in the temperature range of the experiments from  $10^{-26.63}$  at 120°C  
389 to  $10^{-25.42}$  at 200°C (Wang and Nancollas 2008). Considering the very large differences in  
390 solubility between anhydrite and both calcium phosphates, it is likely that the latter phases  
391 form under very high supersaturations and can be expected that this process occurs rapidly at  
392 any experimental temperature. Therefore, anhydrite dissolution is most likely the rate-limiting  
393 process. However, the progress of the reaction requires continuous chemical exchange with  
394 the bulk solution and the rate of mass transport through the porous replaced rim may play a  
395 significant role modulating the overall kinetics of the anhydrite by calcium phosphate  
396 replacement reaction.

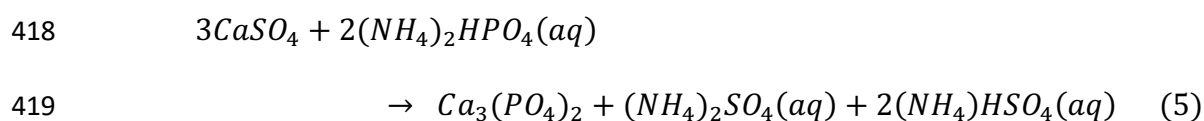
### 397 **Reaction pathway**

398 The mole ratio of  $\beta$ -TCP/Hap vary with temperature and reaction time. At 120°C,  $\beta$ -TCP/Hap  
399 mole ratio first increases with reaction time and later slowly decreases. At all other  
400 temperatures  $\beta$ -TCP/Hap mole ratio progressively decreases with increasing reaction time.  
401 This decrease takes place much more rapidly with increasing temperature. In the temperature  
402 range of the experiments,  $\beta$ -TCP is more soluble than Hap (lInl.dat) and, consequently, less  
403 stable. Therefore,  $\beta$ -TCP forms as a thermodynamically metastable phase. Crystallization of  
404 metastable phases often occurs under high supersaturations. The large solubility difference  
405 between anhydrite,  $\beta$ -TCP and Hap determines that the layer of fluid at the interface will be  
406 very highly supersaturated with respect to both,  $\beta$ -TCP and Hap. Under these conditions, both  
407 calcium phosphate phases can nucleate. Indeed, the presence of Hap at very early stages of  
408 the replacement process suggests a competition between the nucleation and growth of  $\beta$ -TCP  
409 and Hap. Metastable  $\beta$ -TCP latter transforms into Hap according to an Ostwald ripening  
410 process. This transformation most likely occurs through a dissolution-reprecipitation reaction

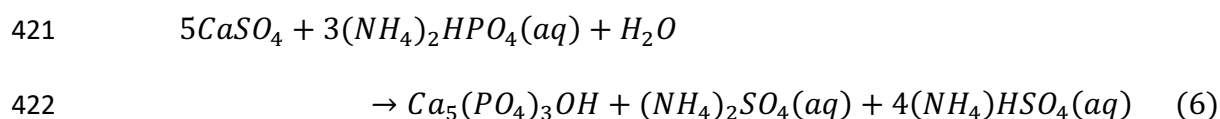
411 since dissolution pits are apparent in the surface of  $\beta$ -TCP and needle-like Hap crystals grow  
412 spatially associated to those pits (Fig. 3b). The competition between the nucleation and growth  
413 of  $\beta$ -TCP and Hap operates longer and plays a more important role at lower temperatures as  
414 is evidenced by the initial increase in the  $\beta$ -TCP/Hap mole ratio as well as the large amount  
415 of  $\beta$ -TCP in almost fully replaced samples at 120°C.

416 The replacement reaction can be described through the following equations:

417



420



423



425

426 The precipitation of Hap, as a basic salt, results in a pH decrease in the fluid phase (equations  
427 6 and 7). This is in good agreement with the change from an initial  $pH_i = 8.1$  (1) to a pH of  
428 6.8 (1) measured at the end of the experiments.

### 429 **Porosity generation**

430 Several factors explain the generation of porosity during pseudomorphic replacement  
431 reactions. Porosity balances the loss of volume in reactions that involve a negative molar  
432 volume change and guarantees the preservation of the original external shape of the primary  
433 phase. In the case of the replacement of anhydrite ( $V_{Anh} = 45.84 \text{ cm}^3/\text{mol}$ ) by mixtures of  $\beta$ -

434 TCP ( $V_{\beta\text{-TCP}} = 33.14$ ) and Hap ( $V_{\text{Hap}} = 31.79 \text{ cm}^3/\text{mol}$ ), all relevant molar volume changes are  
435 negative:  $-12.70 \text{ cm}^3/\text{mol}$  (27,7%) and  $-14.05$  (30.65%), the changes associated to the  
436 transformation of anhydrite into  $\beta$ -TCP and Hap, respectively, and  $-1.35$  (4.07%) the change  
437 associated to the transformation of  $\beta$ -TCP into Hap. These molar volume changes only very  
438 slightly vary ( $< 1\%$ ) depending on the experimental temperature (Evans 1979; Nakamura et  
439 al. 1990). The porosity required to balance the molar volume change associated to the  
440 replacement reaction will be around 30%, although the exact value will vary depending on the  
441  $\beta$ -TCP/Hap mole ratio in the calcium phosphate mixture. Since this ratio changes with reaction  
442 time and temperature, small differences in porosity can be expected depending on the  
443 experimental conditions.

444 A second source of porosity is the difference in solubility between the primary and product  
445 phases (Putnis 2002, 2009; Pollok et al. 2011).  $\beta$ -TCP and Hap are less soluble than anhydrite.  
446 This means that part of the dissolved anhydrite is lost to the solution when this phase is  
447 replaced by  $\beta$ -TCP and Hap. The negative solubility change associated to the replacement will  
448 also be balanced by generation of porosity that will add up to that that balances the negative  
449 molar volume change. The volume of solubility change-related porosity is also influenced by  
450 reaction time and temperature as both parameters determine the  $\beta$ -TCP/Hap in the reacted  
451 sample. Differences in the porosity formed during the replacement may influence the mass  
452 transport rate and be reflected by the overall kinetics of the replacement reaction (Jonas et al.  
453 2013; Pedrosa et al. 2017).

#### 454 **Textural features and evolution**

455 Mass transport from and to the interface is not only affected by the increase of porosity during  
456 the replacement but also by the specific characteristics of this porosity regarding pore shape,  
457 size and connectivity (Putnis et al. 2005; Jonas et al. 2013; Putnis 2015; Yuan et al. 2018;  
458 Forjanés et al. 2020a). Yuan et al. (2018) studied the porosity generated during the

459 replacement of calcite by cerussite and identified three types of pores: Open pores that directly  
460 connect the reaction front and the bulk solution, trapped pores, which are connected through  
461 grain boundary diffusion between the crystals of the product phase and open pores to the bulk  
462 solution, and isolated pores, located between differently oriented crystals of the product. All  
463 types of pores are filled by fluid, but the chemistry of this fluid will vary due to differences in  
464 the mass transport rate. Chemical exchange between the interfacial fluid and the bulk will be  
465 more efficient if the porosity mainly consists of open pores, while the predominance of  
466 isolated pores will strongly hinder mass transport and the progress of the reaction. Both habit  
467 and textural relationships of the product crystals are key features that define the relative  
468 amount of open, trapped and isolated pores in replaced samples. The existence/absence of  
469 epitactic relationships between the product and the primary phase is another key factor. We  
470 observe no evidence of epitatic growth of either  $\beta$ -TCP or Hap on anhydrite surfaces.  $\beta$ -TCP  
471 crystals grow randomly oriented, while Hap grow as fan-like bunches of needle-like crystals  
472 arranged approximately perpendicular to the anhydrite surface (Fig. 3).  $\beta$ -TCP crystals  
473 accumulated in the central region of this bunches. Needle-like crystals within bunches that  
474 seem to originate at the region occupied by  $\beta$ -TCP crystals are arranged with their long axis  
475 approximately parallel between them. This arrangement is characteristic of competitive  
476 growth between crystals that nucleate randomly oriented on a surface and have a preferential  
477 growth direction. Those crystals oriented with the preferential growth direction perpendicular  
478 to the surface can grow freely, while the growth of all differently oriented crystals rapidly  
479 becomes prevented by the lack of space. It is noteworthy that the porosity generated during  
480 replacement reactions has a transient nature, and its features evolve along time. In the case of  
481 the replacement of anhydrite by calcium phosphate, the very different habit of  $\beta$ -TCP and Hap  
482 crystals will determine differences in the relative abundance of different types of pores  
483 depending on the mole  $\beta$ -TCP/Hap ratio in the replaced sample. As pores between elongated,

484 parallel crystals tend to be open, it can be expected that the number of open pores in replaced  
485 samples will increase as more  $\beta$ -TCP transforms into Hap.

#### 486 **Rate-limiting process**

487 Coupled dissolution-precipitation reactions are heterogeneous processes. Their kinetics is  
488 either limited by the dissolution of the primary phase or by the precipitation of the product  
489 phase(s). Several observations give support to the interpretation that the dissolution of  
490 anhydrite is the limiting step of the anhydrite by calcium phosphate replacement reaction  
491 Moreover, textural features of the reacted samples indicate that the reaction progresses from  
492 rim to core. This has been interpreted by different authors as evidence of the precipitation of  
493 the product(s) taking place at a faster rate than the dissolution of the primary phase. Altree-  
494 Williams et al. (2015, 2017) pointed out that mineral replacement reactions which are rate-  
495 limited by the precipitation of the product also result in the formation of pseudomorphs.  
496 However, external features of these pseudomorphs are less accurately preserved as the  
497 formation of overgrowths blurs them. Moreover, these pseudomorphs show hollow cores.  
498 Neither the development of overgrowths nor the formation of a hollow core is observed during  
499 the formation of calcium phosphate pseudomorphs after anhydrite.

500 Altree-Williams et al. (2019) calculated an average empirical activation energy ( $E_a$ ) of  $46.2 \pm$   
501  $7.6$  kJ/mol for the carbonation of anhydrite. These authors interpreted the slightly lower value  
502 of this activation energy compared to previously reported values of the activation energy for  
503 anhydrite dissolution [ $50$  kJ/mol, Bildstein et al. (2001);  $61.0 \pm 1.0$  kJ/mol, Kontrec et al.  
504 (2002)] as indicative of anhydrite dissolution being the rate-limiting event of anhydrite  
505 carbonation kinetics. Moreover, they concluded that, since the reported values of the  
506 activation energy for the diffusion of dissolved calcium are much smaller ( $E_a = 12.6$  kJ/mol),  
507 mass transport of species from the bulk solution to the reaction interface and backwards must  
508 occur a faster rate compared to anhydrite dissolution. The average empirical activation energy

509 of the anhydrite by calcium phosphate replacement reaction determined in this work using the  
510 isoconversional method is  $39.9 \pm 1.6$  kJ/mol. The similarity of this value to the previously  
511 reported activation energy for anhydrite carbonation supports that anhydrite dissolution also  
512 controls the kinetics of anhydrite phosphation.

513 The experimental data fitted the Avrami model yields an  $E_a = 40.2 \pm 1.9$  kJ/mol, which is  
514 identical to that obtained using the isoconversional method regardless of the transformed  
515 fraction considered. The calculated  $A$  is  $9045.3$  (hours)<sup>-1</sup> and the resulting integral law is  $Y_{CaP}$   
516  $= 9045.3e^{(-40/RT)t}$ . Applying the law equation and assuming that the reaction mechanism is  
517 the same as that controlling the process in the 120-200°C range, it can be estimated that at  
518 20°C the time required to for the complete replacement of anhydrite single crystals by calcium  
519 phosphate will be around 4 months. However, similar experiments performed under lower  
520 temperature conditions need to be performed to confirm the soundness of this approach.

521 The shape of the rate curves in Figure 5 is approximately the same for those corresponding to  
522 150°C, 180°C and 200°C and the curves can be described as isokinetic. Consistently, the  
523 Avrami reaction exponents ( $n$ ) corresponding to these three temperatures show almost  
524 identical values ( $\sim 1.35$ ). The shape of the rate curve corresponding to 120°C is slightly  
525 different, which correlates with a larger Avrami exponent ( $\sim 1.66$  at 120°C) (Fig. 5). The value  
526 of Avrami exponents is characteristic of the rate-limiting kinetic mechanism that operates at  
527 each temperature (Redfern 1987). All calculated Avrami exponents in this work stand between  
528 those defined by Hancock and Sharp (1972) for first-order and higher-order processes.  
529 However, it is important to keep into mind that Hancock and Sharp (1972) studied solid-state  
530 transformations, while the replacement of anhydrite by calcium phosphate phase takes place  
531 mediated by the presence of a fluid phase. Several authors have interpreted changes in the  
532 value of the Avrami exponent with temperature as reflecting a balance between changes in the  
533 solubilities of the primary and secondary phases combined with changes that affect mass

534 transport processes (Zhao et al. 2009; Aitree-Williams et al. 2019). The solubility of anhydrite  
535 and apatite decrease with increasing temperature. However, this decrease follows a different  
536 trend depending on the phase (Gregory et al. 1974; McDowell et al. 1977; Otálora and García-  
537 Ruiz 2014; Inl database from PHREEQC code). Moreover, in the temperature range of the  
538 experiments the solubility of  $\beta$ -TCP shows a positive dependence with temperature. These  
539 differences in solubility evolution may be reflected by the Avrami exponent. Anhydrite  
540 phosphation does not only involve the dissolution of anhydrite to form Hap.  $\beta$ -TCP  
541 precipitation is metastable and, as the reaction progresses,  $\beta$ -TCP dissolves to form Hap. The  
542 formation of  $\beta$ -TCP and its transformation into Hap may also weigh differently on the overall  
543 kinetics of the replacement depending on the reaction temperature. Reported values of the  
544 empirical activation energy of  $\beta$ -TCP dissolution are around 16.3 kJ/mol, which is much  
545 smaller a value than that of the activation energy for the dissolution of anhydrite and very  
546 close to the activation energy for the diffusion of dissolved calcium (Bohner et al. 1997).  
547 Although its activation energy is small, the influence of  $\beta$ -TCP dissolution may sufficiently  
548 influence the kinetics of Hap formation as to explain changes in the Avrami exponent.  
549 Moreover, the  $\beta$ -TCP into Hap transformation differently affect textural features of the  
550 reacted samples depending on the temperature. After complete replacement of anhydrite by  
551 calcium phosphate,  $\beta$ -TCP content is highest in samples reacted at 120°C (~20%), followed  
552 by those reacted at 150°C (~13%). Given the very different morphology of  $\beta$ -TCP crystals  
553 compared to those of hydroxyapatite as well as the slightly larger molar volume of the former,  
554 differences in porosity and pores arrangement may further explain small kinetics changes at  
555 different reaction temperatures (Putnis et al. 2005; Jonas et al. 2013; Putnis 2015; Pedrosa et  
556 al. 2017).

557

## 558 **Implications**

559 In this work we have analysed the kinetics of the replacement of anhydrite single crystals by  
560 mixtures of the calcium phosphates phases,  $\beta$ -TCP and Hap, *via* a dissolution-precipitation  
561 reaction that takes place under hydrothermal conditions (from 120 to 200°C). The fitting of  
562 the experimental results to both, the Avrami equation and the isoconversional method yields  
563 experimental activation energies,  $E_a$ , around 40 kJ/mol. This value is similar to that  
564 determined by Aitree-Williams et al. (2019) for the carbonation of anhydrite, which is rate-  
565 limited by anhydrite dissolution. However, Avrami exponents stand between those defined  
566 by Hancock and Sharp (1972) for first-order and higher-order processes. We interpret that this  
567 apparent contradiction reflects the complexity of coupled dissolution-precipitation reactions,  
568 whose kinetics is modulated by a number of factors, including the dissolution rate of the  
569 primary phase, the volume, connectivity and permeability of the porosity formed during the  
570 replacement, the precipitation rate of the secondary phase(s) and the textural evolution of the  
571 latter. In the case under consideration, we conclude that there exists a competition between  
572 the nucleation and growth of  $\beta$ -TCP and Hap at early stages of the replacement, which last  
573 longer the lower the reaction temperature is. Due to the very different morphological features  
574 of  $\beta$ -TCP and Hap crystals, this competition strongly influences the texture of the replacement,  
575 its pores arrangement and, thereby, mass transfer from and to the interfacial fluid, emphasizing  
576 the important role of metastable precursor phases and Ostwald ripening processes in defining  
577 the overall kinetics of coupled dissolution-precipitation reactions. The results of this study  
578 indicated that the replacement of sedimentary rock-forming minerals during diagenesis is a  
579 feasible mechanism for the formation of some calcium phosphate accumulations in  
580 sedimentary basins. In this study anhydrite single crystals were used. Anhydrite sedimentary  
581 rocks are polycrystalline materials that consist of grains bounded by differently oriented  
582 crystal surfaces. The reactivity of these surfaces may differ from that of the anhydrite cleavage  
583 surfaces. Moreover, the presence of differently oriented crystal surfaces may facilitate the

584 epitactic growth of the product phases on the parent phase substrate. It is well established that  
585 the formation of epitactic overgrowths contributes to passivate the substrate and commonly  
586 hinders the progress of replacement reactions (Rodríguez-Blanco et al. 2007; Forjanés et al.  
587 2020a). On the other hand, the network of grain boundaries in rocks facilitates fluid infiltration  
588 and provides an increased reactive surface compared to single crystal, which may influence  
589 the reaction mechanism (Jonas et al. 2013, 2014). Future experimental work using anhydrite  
590 evaporitic rock samples will help to elucidate this influence. The results of this study also shed  
591 light on the mechanisms involved in the removal and immobilization of an important  
592 pollutant, P, by mineral surfaces. Due to the main role of P in the life cycle, the scarcity of  
593 this element in the Earth's crust and its ability to pollute soils, sediments and ground and  
594 running waters, developing methods for the recovery of P through the precipitation of  
595 phosphate phases on the surface of pre-existing minerals would have an outstanding  
596 importance. The results of this study together to further experimental work using  
597 polycrystalline samples and fluids with P concentrations closer to those found in natural  
598 environments can contribute to reach this goal.

599

## 600 **Acknowledgements**

601 This study was supported by the Ministry of Science, Innovation and Universities (CIENCIA)  
602 (Spain) under projects CGL2016-77138-C2-1-P, CGL2016-77138-C2-2-P and PID2021-  
603 125467NB-I00. AR acknowledges funding through contract BES-2017-081759 from the  
604 Spanish Science Ministry. The authors thank Emilio Matesanz (CAI Rayos X, Complutense  
605 University of Madrid) and the SCTs (University of Oviedo) for providing excellent technical  
606 support and assistance.

607

608

609 **References**

610 Altree-Williams, A., Pring, A., Ngothai, Y., and Brugger, J. (2015) Textural and  
611 compositional complexities resulting from coupled dissolution–reprecipitation  
612 reactions in geomaterials. *Earth-Science Reviews*, 150, 628–651.

613 Altree-Williams, A., Pring, A., Ngothai, Y., and Brugger, J. (2017) The Carbonatation of  
614 Anhydrite: Kinetics and Reaction Pathways. *ACS Earth and Space Chemistry*, 1, 89–  
615 100.

616 Altree-Williams, A., Brugger, J., Pring, A., and Bedrikovetsky, P. (2019) Coupled reactive  
617 flow and dissolution with changing reactive surface and porosity. *Chemical  
618 Engineering Science*, 206, 289–304.

619 Baturin, G. (1989) The origin of marine phosphorites. *International Geology Review*, 31, 327–  
620 342.

621 Bentor, Y. (1980) Phosphorites—the unsolved problems. In *Marine Phosphorites-  
622 Geochemistry, Occurrence, Genesis* Vol. 29, pp. 3–18. SEPM Society for Sedimentary  
623 Geology, Tulsa.

624 Bildstein, O., Worden, R., and Brosse, E. (2001) Assessment of anhydrite dissolution as the  
625 rate-limiting step during thermochemical sulfate reduction. *Chemical geology*, 176,  
626 173–189.

627 Bohner, M., Lemaître, J., and Ring, T.A. (1997) Kinetics of dissolution of  $\beta$ -tricalcium  
628 phosphate. *Journal of colloid and interface science*, 190, 37–48.

- 629 Callagon, E.B.R., Lee, S.S., Eng, P.J., Laanait, N., Sturchio, N.C., Nagy, K.L., and Fenter, P.  
630 (2017) Heteroepitaxial growth of cadmium carbonate at dolomite and calcite surfaces:  
631 Mechanisms and rates. *Geochimica et Cosmochimica Acta*, 205, 360–380.
- 632 Di Lorenzo, F., Ruiz-Agudo, C., and Churakov, S.V. (2019) The key effects of polymorphism  
633 during Pb II uptake by calcite and aragonite. *CrystEngComm*, 21, 6145–6155.
- 634 Dzombak, R.M., and Sheldon, N.D. (2020) Weathering Intensity and Presence of Vegetation  
635 Are Key Controls on Soil Phosphorus Concentrations: Implications for Past and Future  
636 Terrestrial Ecosystems. *Soil Systems*, 4.
- 637 Evans, H.T. (1979) The thermal expansion of anhydrite to 1000°C. *Physics and Chemistry of*  
638 *Minerals*, 4, 77–82.
- 639 Ewing, R.C., and Wang, L. (2002) Phosphates as nuclear waste forms. *Reviews in mineralogy*  
640 *and geochemistry*, 48, 673–699.
- 641 Filippelli, G.M. (2002) The Global Phosphorus Cycle. *Reviews in Mineralogy and*  
642 *Geochemistry*, 48, 391–425.
- 643 Forjanés, P., Gómez-Barreiro, J., Morales, J., Astilleros, J.M., and Fernández-Díaz, L. (2020a)  
644 Epitactic growth of celestite on anhydrite: substrate induced twinning and  
645 morphological evolution of aggregates. *CrystEngComm*, 22, 5743–5759.
- 646 Forjanés, P., Astilleros, J.M., and Fernández-Díaz, L. (2020b) The Formation of Barite and  
647 Celestite through the Replacement of Gypsum. *Minerals*, 10, 189.
- 648 Freyer, D., and Voigt, W. (2003) Crystallization and Phase Stability of CaSO<sub>4</sub> and CaSO<sub>4</sub> –  
649 Based Salts. *Monatshefte für Chemie / Chemical Monthly*, 134, 693–719.

- 650 Gopal, R., and Calvo, C. (1972) Structural relationship of whitlockite and  $\beta\text{Ca}_3(\text{PO}_4)_2$ . Nature  
651 Physical Science, 237, 30–32.
- 652 Gregory, T., Moreno, E., Patel, J., and Brown, W. (1974) Solubility of  $\beta\text{-Ca}_3(\text{PO}_4)_2$  in the  
653 system  $\text{Ca}(\text{OH})_2\text{-H}_3\text{PO}_4\text{-H}_2\text{O}$  at 5, 15, 25, and 37°C. J Res Natl Bur Stand 78:667-674.  
654 Journal of Research of the National Bureau of Standards. Section A, Physics and  
655 Chemistry, 78, 667.
- 656 Hancock, J.D., and Sharp, J.H. (1972) Method of Comparing Solid-State Kinetic Data and Its  
657 Application to the Decomposition of Kaolinite, Brucite, and  $\text{BaCO}_3$ . Journal of the  
658 American Ceramic Society, 55, 74–77.
- 659 Hawthorne, F., and Ferguson, R. (1975) Anhydrous sulphates; II, Refinement of the crystal  
660 structure of anhydrite. The Canadian Mineralogist, 13, 289–292.
- 661 Hövelmann, J., and Putnis, C.V. (2016) In situ nanoscale imaging of struvite formation during  
662 the dissolution of natural brucite: implications for phosphorus recovery from  
663 wastewaters. Environmental Science & Technology, 50, 13032–13041.
- 664 Hughes, J.M., Cameron, M., and Crowley, K.D. (1989) Structural variations in natural F, OH,  
665 and Cl apatites. American Mineralogist, 74, 870–876.
- 666 Jonas, L., John, T., and Putnis, A. (2013) Influence of temperature and Cl on the hydrothermal  
667 replacement of calcite by apatite and the development of porous microstructures.  
668 American Mineralogist, 98, 1516–1525.
- 669 Jonas, L., John, T., King, H.E., Geisler, T., and Putnis, A. (2014) The role of grain boundaries  
670 and transient porosity in rocks as fluid pathways for reaction front propagation. Earth  
671 and Planetary Science Letters, 386, 64–74.

- 672 Kasioptas, A., Geisler, T., Putnis, C.V., Perdikouri, C., and Putnis, A. (2010) Crystal growth  
673 of apatite by replacement of an aragonite precursor. *Journal of Crystal Growth*, 312,  
674 2431–2440.
- 675 Kasioptas, A., Geisler, T., Perdikouri, C., Trepmann, C., Gussone, N., and Putnis, A. (2011)  
676 Polycrystalline apatite synthesized by hydrothermal replacement of calcium  
677 carbonates. *Geochimica et Cosmochimica Acta*, 75, 3486–3500.
- 678 Kaufman, H.W., and Kleinberg, I. (1979) Studies on the incongruent solubility of  
679 hydroxyapatite. *Calcified Tissue International*, 27, 143.
- 680 Knudsen, A.C., and Gunter, M.E. (2002) Sedimentary Phosphorites—An Example:  
681 Phosphoria Formation, Southeastern Idaho, U.S.A. *Reviews in Mineralogy and*  
682 *Geochemistry*, 48, 363–389.
- 683 Kontrec, J., Kralj, D., and Brečević, L. (2002) Transformation of anhydrous calcium sulphate  
684 into calcium sulphate dihydrate in aqueous solutions. *Journal of Crystal Growth*, 240,  
685 203–211.
- 686 Kuhn, T., Herzig, P.M., Hannington, M.D., Garbe-Schönberg, D., and Stoffers, P. (2003)  
687 Origin of fluids and anhydrite precipitation in the sediment-hosted Grimsey  
688 hydrothermal field north of Iceland. *Chemical Geology*, 202, 5–21.
- 689 Lasaga, A.C. (1998) *Kinetic theory in the earth sciences* Vol. 811. Princeton, NJ: Princeton  
690 university press.
- 691 Li, M., Wang, L., Zhang, W., Putnis, C.V., and Putnis, A. (2016) Direct Observation of Spiral  
692 Growth, Particle Attachment, and Morphology Evolution of Hydroxyapatite. *Crystal*  
693 *Growth & Design*, 16, 4509–4518.

- 694 Mallin, M.A., and Cahoon, L.B. (2020) The Hidden Impacts of Phosphorus Pollution to  
695 Streams and Rivers. *BioScience*, 70, 315–329.
- 696 Mavropoulos, E., Rossi, A.M., Costa, A.M., Perez, C.A.C., Moreira, J.C., and Saldanha, M.  
697 (2002) Studies on the Mechanisms of Lead Immobilization by Hydroxyapatite.  
698 *Environmental Science & Technology*, 36, 1625–1629.
- 699 McDowell, H., Gregory, T.M., and Brown, W.E. (1977) Solubility of  $\text{Ca}_5(\text{PO}_4)_3\text{OH}$  in the  
700 System  $\text{Ca}(\text{OH})_2\text{-H}_3\text{PO}_4\text{-H}_2\text{O}$  at 5, 15, 25, and 37°C. *Journal of Research of the*  
701 *National Bureau of Standards. Section A, Physics and Chemistry*, 81A, 273–281.
- 702 Morales, J., Astilleros, J.M., Jiménez, A., Göttlicher, J., Steininger, R., and Fernández-Díaz,  
703 L. (2014) Uptake of dissolved lead by anhydrite surfaces. *Applied Geochemistry*, 40,  
704 89–96.
- 705 Murray, R.C. (1964) Origin and diagenesis of gypsum and anhydrite. *Journal of Sedimentary*  
706 *Research*, 34, 512–523.
- 707 Nakamura, S., Otsuka, R., Aoki, H., Akao, M., Miura, N., and Yamamoto, T. (1990) Thermal  
708 expansion of hydroxyapatite- $\beta$ -tricalcium phosphate ceramics. *Thermochimica Acta*,  
709 165, 57–72.
- 710 Olivarius, M., Weibel, R., Hjuler, M.L., Kristensen, L., Mathiesen, A., Nielsen, L.H., and  
711 Kjøller, C. (2015) Diagenetic effects on porosity–permeability relationships in red  
712 beds of the Lower Triassic Bunter Sandstone Formation in the North German Basin.  
713 *Sedimentary Geology*, 321, 139–153.
- 714 Otálora, F., and García-Ruiz, J. (2014) Nucleation and growth of the Naica giant gypsum  
715 crystals. *Chemical Society Reviews*, 43, 2013–2026.

- 716 Parkhurst, D.L., and Appelo, C. (1999) User's guide to PHREEQC (Version 2): A computer  
717 program for speciation, batch-reaction, one-dimensional transport, and inverse  
718 geochemical calculations. Water-resources investigations report, 99, 312.
- 719 Pedrosa, E.T., Putnis, C.V., and Putnis, A. (2016) The pseudomorphic replacement of marble  
720 by apatite: The role of fluid composition. *Chemical Geology*, 425, 1–11.
- 721 Pedrosa, E.T., Boeck, L., Putnis, C.V., and Putnis, A. (2017) The replacement of a carbonate  
722 rock by fluorite: Kinetics and microstructure. *American Mineralogist*, 102, 126–134.
- 723 Penel, G., Leroy, G., Rey, C., and Bres, E. (1998) MicroRaman Spectral Study of the PO<sub>4</sub> and  
724 CO<sub>3</sub> Vibrational Modes in Synthetic and Biological Apatites. *Calcified Tissue*  
725 *International*, 63, 475–481.
- 726 Pinto, A.J., Jimenez, A., and Prieto, M. (2009) Interaction of phosphate-bearing solutions with  
727 gypsum: Epitaxy and induced twinning of brushite (CaHPO<sub>4</sub>·2H<sub>2</sub>O) on the gypsum  
728 cleavage surface. *American Mineralogist*, 94, 313–322.
- 729 Pinto, A.J., Carneiro, J., Katsikopoulos, D., Jiménez, A., and Prieto, M. (2012) The Link  
730 between Brushite and Gypsum: Miscibility, Dehydration, and Crystallochemical  
731 Behavior in the CaHPO<sub>4</sub>·2H<sub>2</sub>O–CaSO<sub>4</sub>·2H<sub>2</sub>O System. *Crystal Growth & Design*, 12,  
732 445–455.
- 733 Pollok, K., Putnis, C.V., and Putnis, A. (2011) Mineral replacement reactions in solid solution-  
734 aqueous solution systems: Volume changes, reactions paths and end-points using the  
735 example of model salt systems. *American Journal of Science*, 311, 211–236.
- 736 Putnis, A. (1992) *An introduction to mineral sciences*, 457 p. Cambridge University Press.

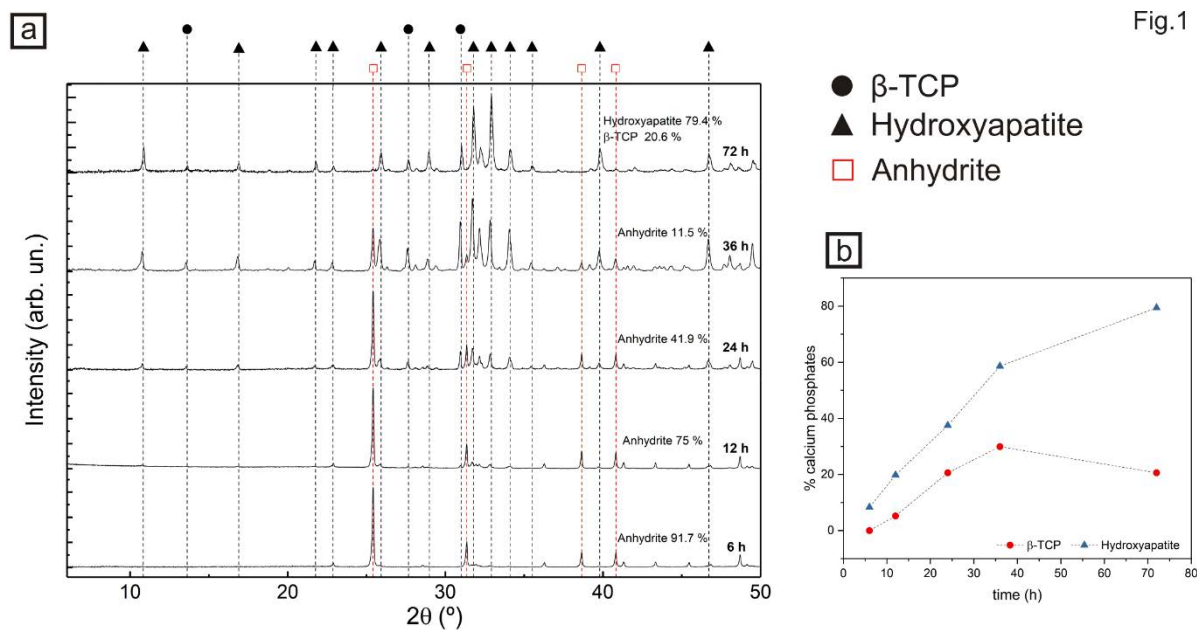
- 737 Putnis, A. (2002) Mineral replacement reactions: from macroscopic observations to  
738 microscopic mechanisms. *Mineralogical Magazine*, 66, 689–708.
- 739 Putnis, A. (2009) Mineral replacement reactions. *Reviews in mineralogy and geochemistry*,  
740 70, 87–124.
- 741 ——— (2015) Transient Porosity Resulting from Fluid–Mineral Interaction and its  
742 Consequences. *Reviews in Mineralogy and Geochemistry*, 80, 1–23.
- 743 Putnis, A., and Putnis, C.V. (2007) The mechanism of reequilibration of solids in the presence  
744 of a fluid phase. *Journal of Solid State Chemistry*, 180, 1783–1786.
- 745 Putnis, C.V., Tsukamoto, K., and Nishimura, Y. (2005) Direct observations of  
746 pseudomorphism: compositional and textural evolution at a fluid-solid interface.  
747 *American Mineralogist*, 90, 1909–1912.
- 748 Rahimpour-Bonab, H., Esrafil-Dizaji, B., and Tavakoli, V. (2010) Dolomitization and  
749 anhydrite precipitation in Permo-Triassic carbonates at the South Pars gas Field,  
750 Offshore Iran: controls on reservoir quality. *Journal of Petroleum Geology*, 33, 43–66.
- 751 Rakovan, J., and Reeder, R.J. (1996) Intracrystalline rare earth element distributions in apatite:  
752 Surface structural influences on incorporation during growth. *Geochimica et*  
753 *Cosmochimica Acta*, 60, 4435–4445.
- 754 Redfern, S.A.T. (1987) The kinetics of dehydroxylation of kaolinite. *Clay Minerals*, 22, 447–  
755 456.
- 756 Reinares-Fisac, D., Veintemillas-Verdaguer, S., and Fernández-Díaz, L. (2017) Conversion  
757 of biogenic aragonite into hydroxyapatite scaffolds in boiling solutions.  
758 *CrystEngComm*, 19, 110–116.

- 759 Rodríguez-Blanco, J.D., Jiménez, A., and Prieto, M. (2007) Oriented Overgrowth of  
760 Pharmacolite ( $\text{CaHAsO}_4 \cdot 2\text{H}_2\text{O}$ ) on Gypsum ( $\text{CaSO}_4 \cdot 2\text{H}_2\text{O}$ ). *Crystal Growth &*  
761 *Design*, 7, 2756–2763.
- 762 Roy, D.M., and Linnehan, S.K. (1974) Hydroxyapatite formed from coral skeletal carbonate  
763 by hydrothermal exchange. *Nature*, 247, 220–222.
- 764 Roza Llera, A., Jimenez, A., and Fernández-Díaz, L. (2021) Removal of Pb from Water: The  
765 Effectiveness of Gypsum and Calcite Mixtures. *Minerals*, 11, 66.
- 766 Ruiz-Agudo, E., Putnis, C.V., and Putnis, A. (2014) Coupled dissolution and precipitation at  
767 mineral–fluid interfaces. *Chemical Geology*, 383, 132–146.
- 768 Ruiz-Agudo, E., Putnis, C.V., Hövelmann, J., Álvarez-Lloret, P., Ibañez-Velasco, A., and  
769 Putnis, A. (2015) Experimental study of the replacement of calcite by calcium  
770 sulphates. *Geochimica et Cosmochimica Acta*, 156, 75–93.
- 771 Sheldon, R.P. (1981) Ancient Marine Phosphorites. *Annual Review of Earth and Planetary*  
772 *Sciences*, 9, 251–284.
- 773 Smith, V.H. (2003) Eutrophication of freshwater and coastal marine ecosystems a global  
774 problem. *Environmental Science and Pollution Research*, 10, 126–139.
- 775 Wang, L., and Nancollas, G.H. (2008) Calcium Orthophosphates: Crystallization and  
776 Dissolution. *Chemical Reviews*, 108, 4628–4669.
- 777 Wang, L., Ruiz-Agudo, E., Putnis, C.V., Menneken, M., and Putnis, A. (2012) Kinetics of  
778 Calcium Phosphate Nucleation and Growth on Calcite: Implications for Predicting the  
779 Fate of Dissolved Phosphate Species in Alkaline Soils. *Environmental Science &*  
780 *Technology*, 46, 834–842.

- 781 Wang, L., Putnis, C.V., Ruiz-Agudo, E., Hövelmann, J., and Putnis, A. (2015) In situ Imaging  
782 of Interfacial Precipitation of Phosphate on Goethite. *Environmental Science &*  
783 *Technology*, 49, 4184–4192.
- 784 Wei, X., and Bailey, R.T. (2021) Evaluating nitrate and phosphorus remediation in intensively  
785 irrigated stream-aquifer systems using a coupled flow and reactive transport model.  
786 *Journal of Hydrology*, 598, 126304.
- 787 Xia, F., Brugger, J., Chen, G., Ngothai, Y., O'Neill, B., Putnis, A., and Pring, A. (2009)  
788 Mechanism and kinetics of pseudomorphic mineral replacement reactions: A case  
789 study of the replacement of pentlandite by violarite. *Geochimica et Cosmochimica*  
790 *Acta*, 73, 1945–1969.
- 791 Yang, Y., Wu, Q., Wang, M., Long, J., Mao, Z., and Chen, X. (2014) Hydrothermal Synthesis  
792 of Hydroxyapatite with Different Morphologies: Influence of Supersaturation of the  
793 Reaction System. *Crystal Growth & Design*, 14, 4864–4871.
- 794 Yuan, K., De Andrade, V., Feng, Z., Sturchio, N.C., Lee, S.S., and Fenter, P. (2018)  $\text{Pb}^{2+}$ -  
795 Calcite Interactions under Far-from-Equilibrium Conditions: Formation of  
796 Micropyramids and Pseudomorphic Growth of Cerussite. *The Journal of Physical*  
797 *Chemistry C*, 122, 2238–2247.
- 798 Zhao, J., Brugger, J., Grundler, P.V., Xia, F., Chen, G., and Pring, A. (2009) Mechanism and  
799 kinetics of a mineral transformation under hydrothermal conditions: Calaverite to  
800 metallic gold. *American Mineralogist*, 94, 1541–1555.
- 801 Zhu, R., Yu, R., Yao, J., Wang, D., and Ke, J. (2008) Morphology control of hydroxyapatite  
802 through hydrothermal process. *Journal of Alloys and Compounds*, 457, 555–559.

803

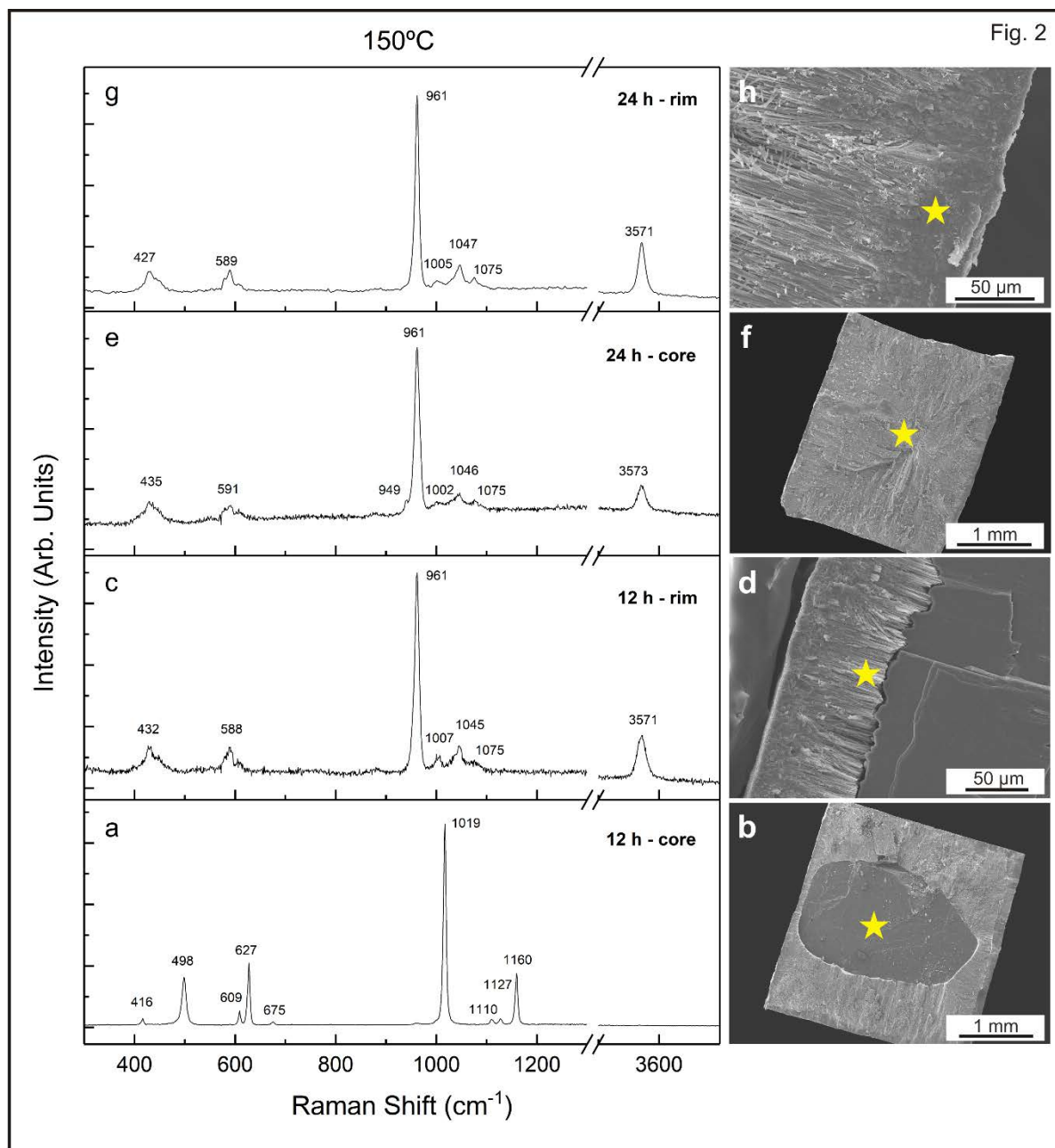
804



805

806 Figure 1. (a) X-ray powder diffraction patterns showing the mineralogical evolution of the  
807 replacement of anhydrite by calcium phosphates after hydrothermal interaction experiments  
808 carried out at 120°C at different reaction times. The reflections of anhydrite, hydroxyapatite  
809 and  $\beta$ -TCP were marked with squares, triangles and circles, respectively. (b) % calcium  
810 phosphates, calculated by Rietveld refinement, against reaction time.

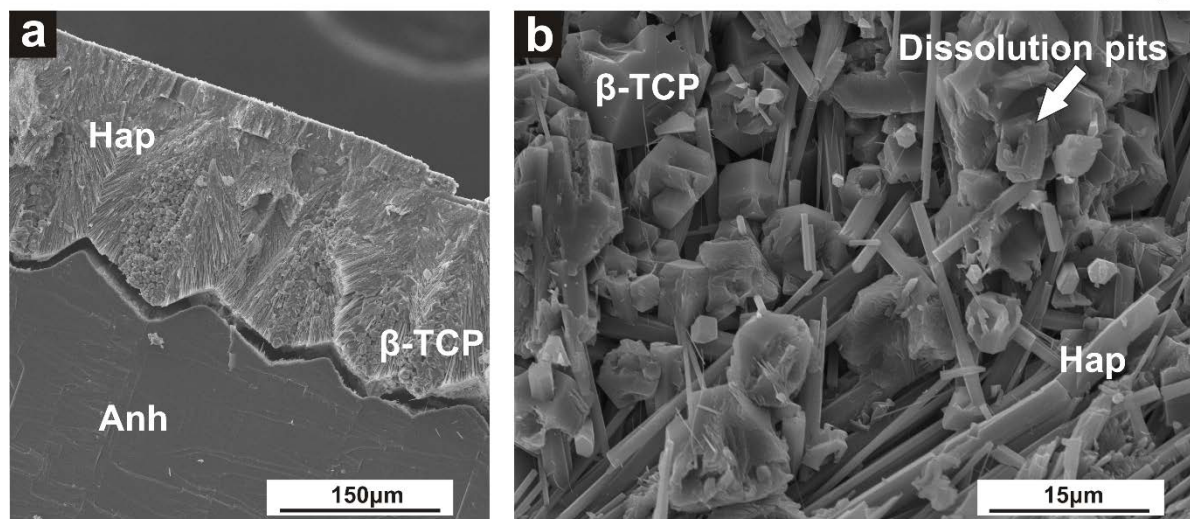
811



812  
813 Figure 2. Raman spectra and SEM images of cross-section of partially replaced anhydrite  
814 samples for 12 h and 24 h at 150°C. The main vibrational bands of SO<sub>4</sub><sup>2-</sup> identified (a) in  
815 the core of anhydrite sample reacted (b) match well with anhydrite. The main vibrational  
816 bands of PO<sub>4</sub><sup>3-</sup> (c, e and g) identified in the rim (d and h) and core (f) of reacted samples  
817 corresponds to hydroxyapatite. The broad band at 949 cm<sup>-1</sup> and the presence of the band at  
818 1045 cm<sup>-1</sup> (d) are characteristic of β-TCP. SEM micrographs of the reacted samples show  
819 the position where the spectra were measured.

820

Fig. 3



821

822

823 Figure 3. SEM micrographs of anhydrite (Anh) reacted with 2M (NH<sub>4</sub>)<sub>2</sub>HPO<sub>4</sub> aqueous

824 solution at different temperatures and reaction times. (a) After 3 h at 150°C a cross cut section

825 image shows the unreacted anhydrite core and the two calcium phosphates that can be

826 distinguished, β-tricalcium phosphate (β -TCP) and hydroxyapatite (Hap). Hydroxyapatite is

827 clearly more abundant and is growing in elongated hexagonal needle-like crystals that are

828 arranged perpendicular to the unreacted anhydrite core and β-TCP shows an euhedral habit.

829 (b) At higher temperatures and shorter reaction times (200°C and 2 h), β -TCP appears with

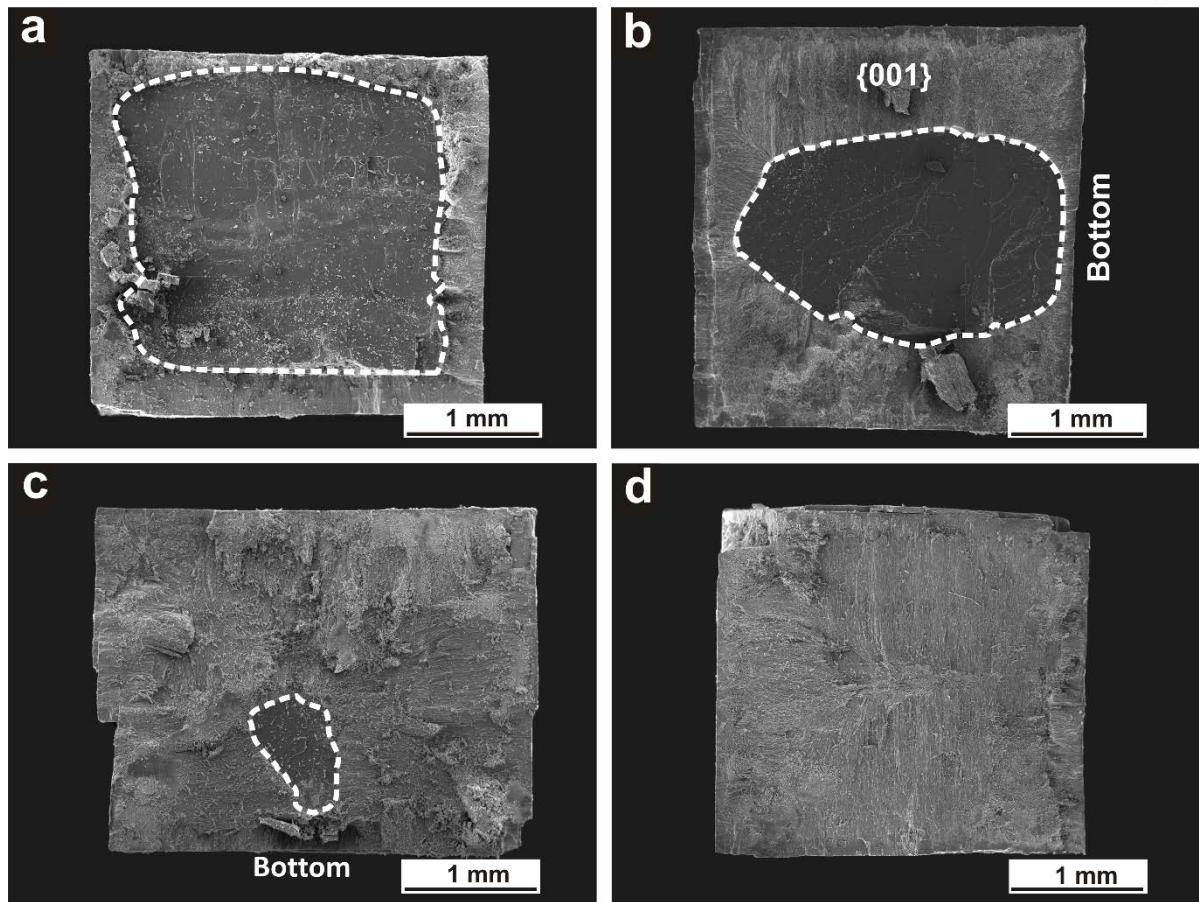
830 dissolution features and at the same time the development of smaller and thinner

831 hydroxyapatite crystals from β -TCP faces.

831

832

Fig. 4

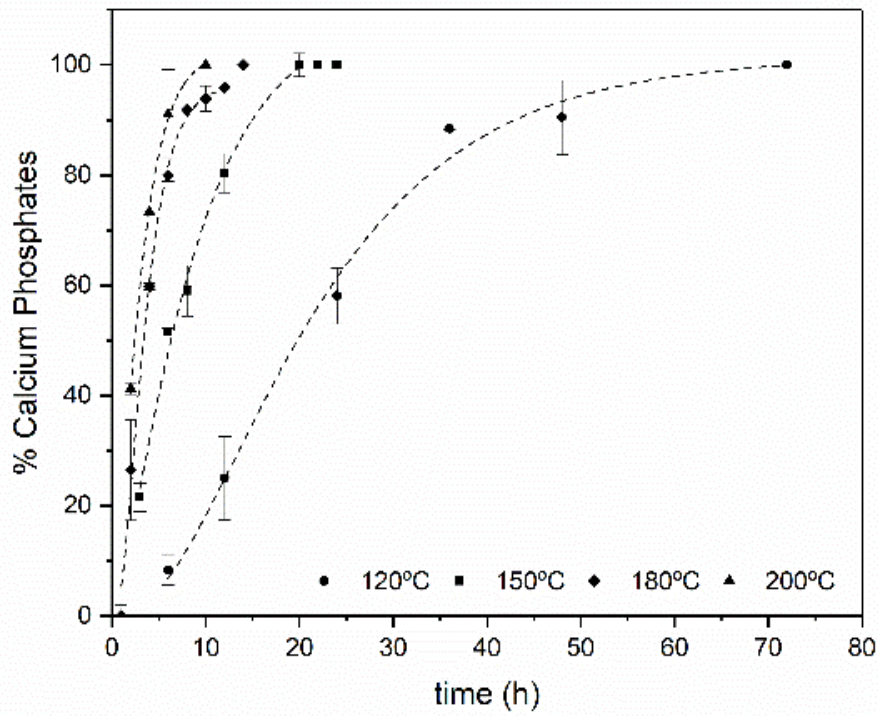


833  
834  
835  
836  
837

Figure 4. SEM micrographs of cross-sections surfaces showing the anhydrite replacement by calcium phosphates after 12 hours of reaction at temperatures of 120 (a), 150 (b), 180 (c) and 200 (d).

838

Fig. 5



839

840 Figure 5. Fraction of calcium phosphates replacing anhydrite crystals against the reaction time  
841 for each isothermal experiments. The lines are fitted to the Chapman equation.

842

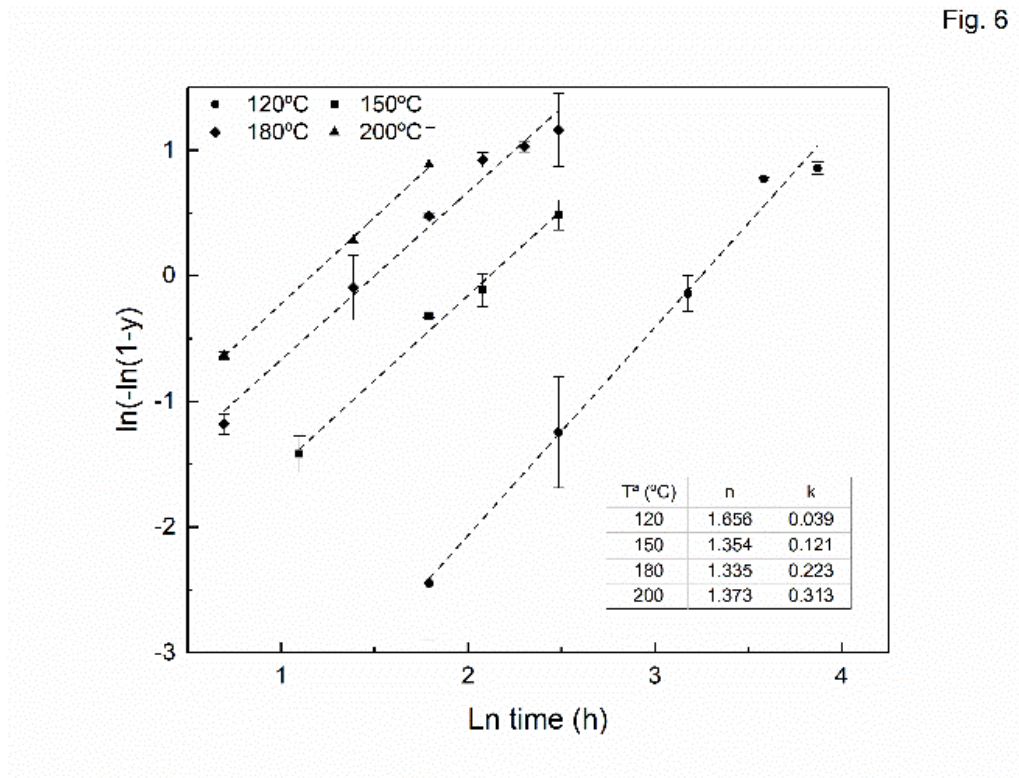
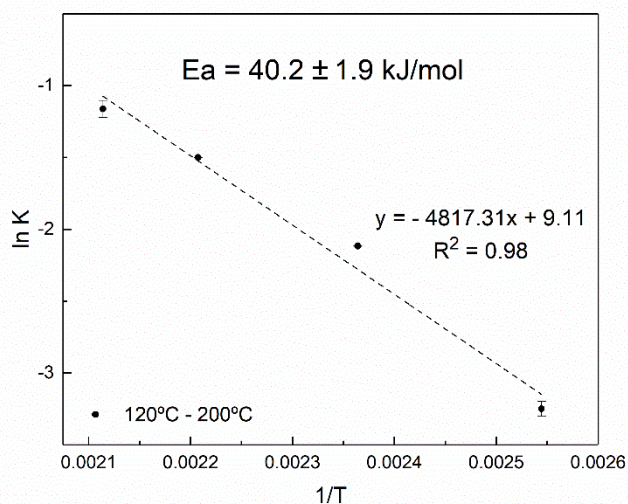


Fig. 6

843

844 Figure 6. Plot of the calcium phosphates transformed fraction (y) versus time. From the slope  
845 and the intercept, Avrami rate law parameters (n and k) are determined.

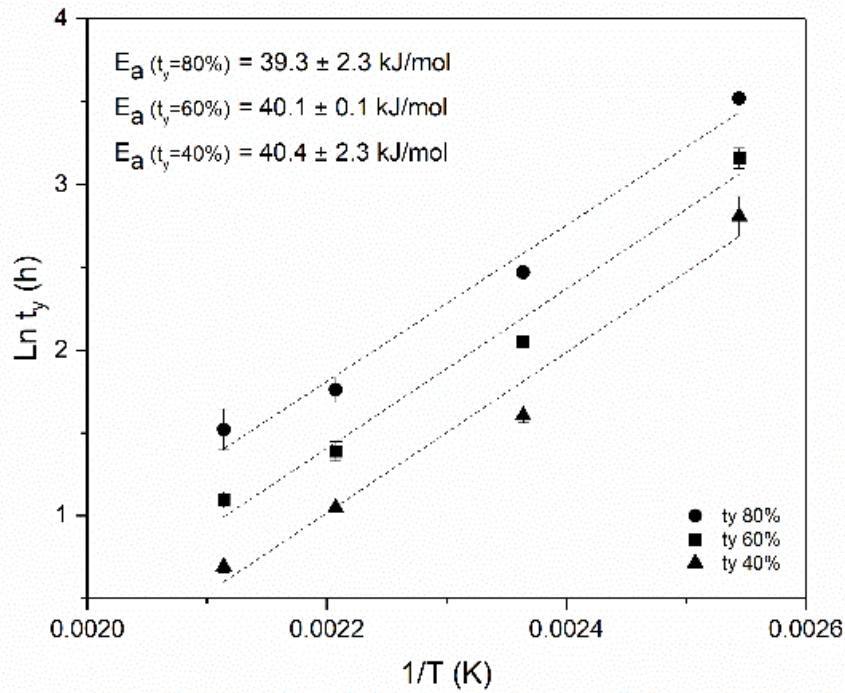
Fig. 7



846 Figure 7. Linear fitting of the rate constant K versus the reciprocal of temperature (expressed  
847 in Kelvin).

848

Fig. 8



849 Figure 8: Experimental data of the time ( $\ln t_y$ ) for several fractions ( $Y=40, 60$  and  $80\%$ ) of  
850 transformed anhydrite versus  $1/T$ . The slope of the fitting straight lines corresponds to  $E_a/R$ .

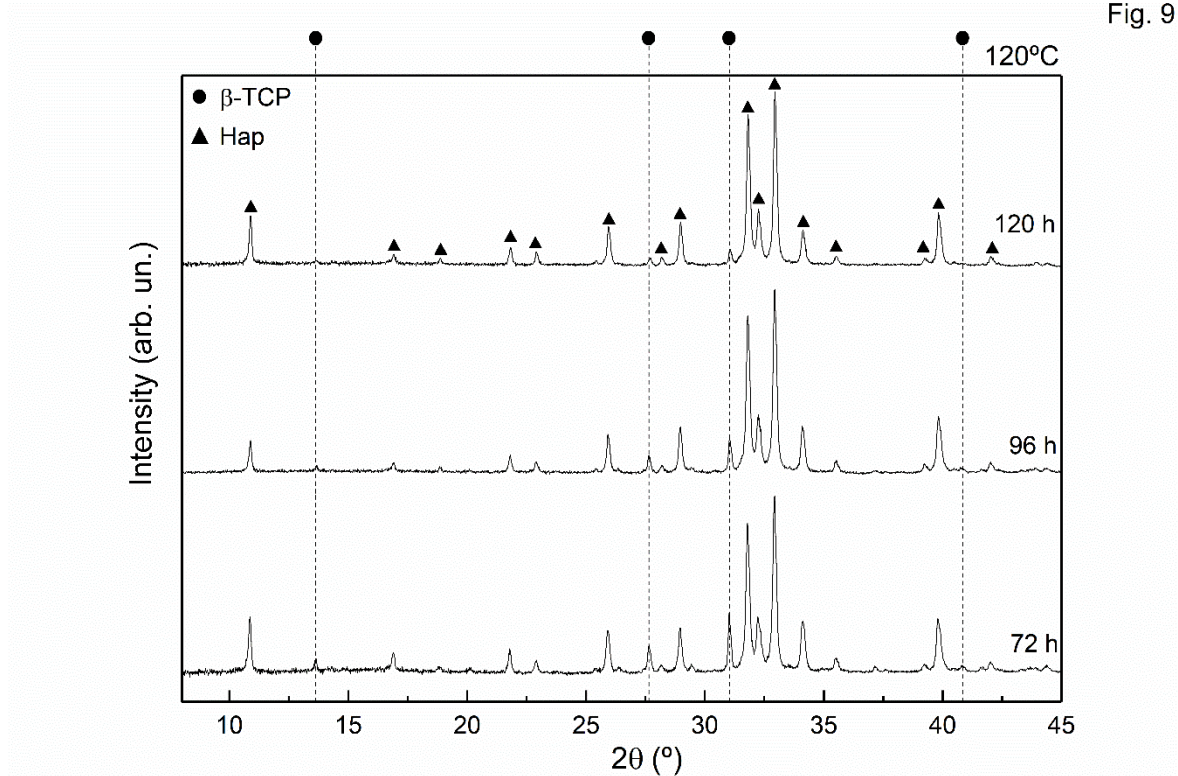
851

852

853 **Supplementary**

854

855



856

857 Figure 9: X-ray powder diffraction patterns showing the mineralogical evolution after  
858 complete replacement of anhydrite at 120°C. The amount of  $\beta$ -TCP continues to decrease with  
859 time.

860

861

120°C				150°C				180°C				200°C			
t (h)	% Anh	% β-TCP	% Hap	t (h)	% Anh	% β-TCP	% Hap	t (h)	% Anh	% β-TCP	% Hap	t (h)	% Anh	% β-TCP	% Hap
6	91.7		8.3	3	78.5	3.2	18.3	2	73.5	12.9	13.6	2	58.8	27.1	14.1
12	75	5.2	19.8	6	48.4	20.4	31.3	4	40.3	21.9	37.9	4	26.8	6.6	66.7
24	41.9	20.6	37.5	8	41	22.5	36.5	6	20	16.7	63.3	6	8.9	4.4	86.7
36	11.5	29.9	58.6	12	19.8	21.1	59.2	8	8.2	7.7	84.2	10	0	0	100
48	9.5	17.2	73.3	20	0	13.5	86.5	10	6.1	3.9	90				
72		20.6	79.4					12	4.1	2	93.9				
								14	0	0	100				

\*  $R_{wp}$  is approximately 10% in all refinements.

862

863 Table 1. Calculated transformation (% calcium phosphates) calculated by Rietveld refinement of X-ray diffraction patterns during hydrothermal  
 864 experiment.

865